Dynamics of Water Droplets in a Counterflow Field and their Effect on Flame Extinction

A. M. LENTATI and H. K. CHELLIAH*

Department of Mechanical, Aerospace and Nuclear Engineering, University of Virginia, Charlottesville, VA 22903

The effect of fine-water droplets in extinguishing steady, laminar counterflow methane-air nonpremixed flames is investigated here, using a numerical approach. A new two-phase model using a hybrid Eulerian-Lagrangian formulation for the gas-droplet flow is developed as part of this work. A key feature of the model developed is that it can avoid the singularity associated with the droplet number density equation in a consistent manner by using a Lagrangian equation for droplet flux fraction. The gas phase is described by a detailed model involving full chemical kinetics and transport, whereas droplet evaporation and heat transfer are modeled assuming quasisteady conditions. Application of the model to several monodisperse sizes of water droplets, ranging from 5–50 μm, revealed an interesting nonmonotonic dependence of the flame extinction strain rate on droplet size. This phenomenon is attributed to the droplet dynamics in the counterflow field considered here and to the resulting nonmonotonic heat sink associated with mass evaporation observed at the oxygen consumption or radical production layer of the flame. © 1998 by The Combustion Institute

INTRODUCTION

Automatic water sprinklers, with a typical mass median drop size of about 750 μm, are extensively used as fire-suppressing devices in certain types of fires (e.g., building fires). Recently, however, fine-water droplets or *water-mist systems* with drop sizes less than 100 μm are being considered as a replacement for recently banned halon 1301 (bromotrifluoromethane — CF_3Br, one of the most effective chemical agents in suppressing gaseous flames but known to cause ozone depletion in the upper atmosphere [1]). One major advantage of a water-mist system over a traditional sprinkler system is that fine-water droplets with lower settling velocity can suspend in air for much longer periods than larger droplets, hence, its applicability as a gaseous fire suppressant. In addition, thermal concepts are often used to distinguish the effectiveness between the two systems. For example, for the same mass of water, the latent heat of vaporization is much greater than the increase in sensible enthalpy from room temperature to the boiling point. Thus, fine-water droplets are believed to be more effective than larger droplets because of the large surface area to volume ratio leading to rapid evaporation and faster cooling of the hot gases. However, in flows associated with real fires, the two classes of droplets can have very different droplet dynamics, and the above qualitative physical and thermal reasoning may not hold. The urgency for rapid transition from halon 1301 to alternate systems, such as water-mist systems, has forced researchers to rush into applications without detailed understanding of the relative (1) physical effects due to the water droplet size, (2) thermal effects due to heat capacity and latent heat of evaporation, and (3) chemical effects due to enhanced overall three-body recombination reactions and shift in water-gas reactions. The objective of this work is to understand the role of such physical, thermal, and chemical effects and accurately quantify their contributions using a simplified reacting flow field.

Laboratory-scale laminar flames established within the mixing layer of counterflow of fuel and air provide an excellent configuration to analyze the dynamics of such water droplets in a hot reacting environment and to understand the flame extinction mechanism. Except for the effects of turbulence (which can introduce many undesired uncertainties in modelling transport phenomena and turbulence-chemistry interactions), this nonpremixed flow configuration has many important features that are relevant for understanding the extinction mechanism of real fires. The most important feature is the ability to accurately control the flow residence time to

*Corresponding author.

investigate the finite-rate chemistry effects. For this reason alone, numerous theoretical and experimental studies have been performed in counterflow field containing homogeneous reactants and, more recently, heterogeneous reactants in the context of fuel spray combustion. For the first time, Continillo and Sirignano [2] investigated the combustion of monodisperse sized fuel droplets in a counterflow field numerically for three different flow conditions. They also investigated the conditions for validity of the self-similarity approximation generally introduced in solving the conservation equations of the counterflow field. In this initial study of Continillo and Sirignano [2], many limiting approximations on the chemical kinetic model, thermochemical and transport data were used. Hence, no attempt was made to predict the flame extinction phenomena. In a subsequent study, Lacas et al. [3] performed detailed numerical simulations of a similar monodisperse spray containing (1) n-heptane fuel droplets, flowing against air, and (2) liquid oxygen droplets, flowing against gaseous hydrogen. In both these studies [2, 3], the droplets were transported in a carrier gas, and the sizes considered were small enough that they were completely vaporized before reaching the stagnation plane established by the two opposed gaseous streams. In another detailed numerical study, Chen et al. [4] considered the motion of droplets in a nonpremixed counterflow field. They considered both n-heptane and water droplets. For the droplet sizes considered, Chen et al. [4] showed that a droplet can penetrate through the stagnation plane established by the gaseous streams and reverse its trajectory at some point in the opposing side of the flow. This also raised an interesting question on details of the numerical technique that could overcome the singularity associated with the droplet number density equation at the point where the droplet trajectory is reversed (see comments by Li et al. in Ref. [4]).

One major difference between the present work and that of Continillo and Sirignano [2] is the description of the outer frozen flow field. In Ref. [2], the outer flow was described by irrotational or potential flow field, assuming that the fuel and air sources are located infinitely apart, while in the present study a more general rotational flow field is used to describe the finite separation distance between fuel and air nozzles. Consequently, assumptions introduced to simplify the Lagrangian equations for droplets to a self-similar form are slightly different. Recent experiments by Li et al. [5] with methanol fuel sprays have indeed found that the outer flow field lies somewhere between the potential flow and plug flow cases, similar to that found for methane–air gaseous flames [6]. Their experiments [5] using a phase-Doppler particle analyzer (PDPA) have also shown that, near the axis of symmetry, the axial velocity, droplet size, and number density are independent of the radial coordinate, as assumed in the present study.

While the above theoretical and experimental studies have addressed aspects of combustion of fuel sprays in a counterflow field, the present study is focused on addressing the flame extinction mechanism by fine-water droplets in a similar flow field. To our knowledge, only Seshadri [7] performed experiments on extinction condition of counterflow flames with water mist, however, the water droplets generated in that study were so small that they were completely vaporized in the air stream. In parallel with the present theoretical work, an experimental effort is currently under way at the University of Virginia on flame extinction by monodisperse water droplets in the size range of 20–60 μm, but here only the details of the two-phase numerical model developed are reported. The numerical model developed can provide detailed description of the flame structure and an improved understanding of the parameters controlling the extinction phenomena. They can also guide the supporting experiments. The nonpremixed flame considered here is that established by a counterflow of methane and air, with monodisperse-sized fine-water droplets introduced with the air stream. The water droplet loading, or the number density, considered is small (the mass fraction of water in condensed phase is less than 3%) such that the ratio of droplet separation distance to droplet diameter is greater than 20. Thus, the collisional effects between droplets are neglected. The gas-phase chemical reactions are described using an elementary reaction mechanism having 17 species in 39 steps, with variable thermochemical and
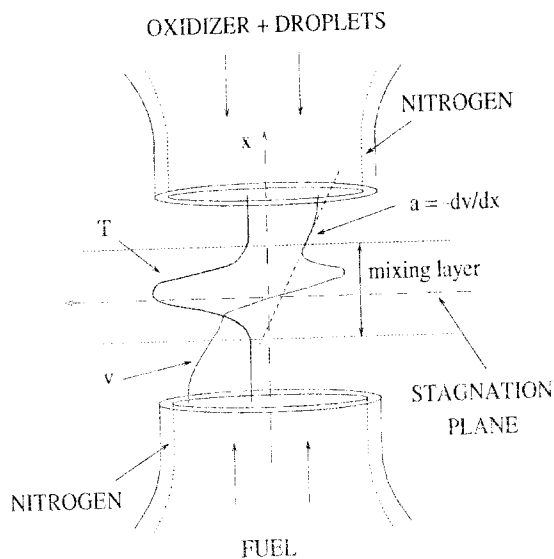
Fig. 1. An illustration of the counterflow field with water droplets. Also shown is the typical gas flow velocity profile, and the definition of flow strain rate used.

transport data. The gas–droplet interaction in the present model is described using hybrid Eulerian–Lagrangian formulation, somewhat similar to that employed in Refs. [2–4]. The discretized gas-phase equations are solved using an algorithm that include Newton and fixed-point iteration steps. Unlike the previous work [4], a rigorous method of handling the singularities associated with the droplet number density equation at the stagnation point of droplets is described. The resulting model is then used to predict the trajectory of water droplets and the modified extinction conditions for a range of monodisperse droplet sizes.

FLOW CONFIGURATION

A schematic of the counterflow configuration considered in the present study, very similar to the ongoing experimental effort, is shown in Fig. 1. When ignited, a steady laminar flame can be established within the mixing layer, as indicated in Fig. 1. The exit velocity profiles of both air and fuel streams are assumed to be of the plug flow type. The droplets are introduced though the upper nozzle at a steady rate with the air stream and are assumed to be monodisperse. In the present simulations, the droplet velocities at

the nozzle exit are assumed to be the same as that of air. In actual experiments, these conditions may differ slightly from those assumed here but can be easily implemented with the two-phase model developed here.

For the two-phase system considered here, the gas velocity can differ from that of droplets. The response of droplet trajectories for different flow strain rates can be addressed by varying the nozzle exit velocities of methane and air streams. For plug flow boundary conditions used here (corresponding to viscous, rotational flow formulation), the flow strain rate, a, is defined as the negative of the axial velocity gradient of the gas in the air side (i.e., $-dv/dx$), just outside the mixing layer, as illustrated in Fig. 1. At flame extinction, the critical value of the flow strain rate is identified here as a_{ext}. In experiments, the outer air flow is known to deviate slightly from the plug flow boundary conditions [6], but, once detailed laser Doppler velocimetry data becomes available, such boundary conditions can be easily implemented in the present model.

FORMULATION

The Navier–Stokes equations, together with multicomponent species and energy conservation equations, are well known and can be found in any text on combustion [8, 9]. With the presence of droplets in the flow, these equations can become rather complicated, but somewhat simplified two-phase conservation equations have already been considered in the context of spray combustion [2–4, 10, 11].

Because of the large density ratio between the liquid and the gas and the low-number density of droplets in the flow, effects of the volume occupied by droplets on the convective and diffusive terms can be easily neglected, with errors introduced being less than 0.1%. As a consequence, interactions between the droplets and gas are only due to source terms associated with transfer of mass, momentum, and energy. Analyses of such couplings can be considerably simplified by assuming that the droplets are monodisperse, as considered here.

Simplified Conservation Equations for the Gas Phase

The gas phase is described by a set of Eulerian equations of conservation of mass, momentum, and energy. The flow is assumed to be axisymmetric, i.e., no swirl, and steady. Because of high flow strain rates considered here, the effects of body forces both in the momentum and in the energy equations are neglected. The gas is a Newtonian fluid, but, due to low Mach number, bulk viscosity effects are neglected. Diffusion velocities are approximated using a simplified multicomponent model. Viscous heating, kinetic energy, work due to gas compression, radiative heat transfer, and Dufour effects are neglected as compared to convective, diffusive, and heat release terms. The condensed phase is assumed to be monocomponent, so that only one of the species equation is affected by its evaporation. The condensed phase effects are averaged as mass, momentum, and enthalpy transfer from the condensed phase to the gas phase per unit volume.

Because the flame established in the mixing layer is planar, a self-similar solution that preserves profiles of scalar variables along the radial direction is used. Thus, we seek a solution of the form [6, 12, 13]

$$v = v(x), \ u = rU(x), \ Y_k = Y_k(x),$$

$$T = T(x), \ p = p(x, r) \tag{1}$$

which becomes exact along the axis of symmetry. Here, x is the axial coordinate, r the radial coordinate, v the mass averaged gas velocity in x direction, u the mass averaged gas velocity in radial direction, Y_k the mass fraction of species k, T the temperature, and p the pressure. For low Mach number flows considered here, pressure is assumed to vary slowly along the axis of symmetry, so that the gas density depends only on the chemical composition and temperature, and the momentum equation along such axis can be eliminated. However, the dependence of pressure in the radial direction cannot be neglected a priori and is given by $p = p_0(x) + r^2 \partial^2 p / \partial r^2$ [14]. Hence, the equation for radial momentum described below must be retained.

In the absence of droplets, such self-similar formulations have been widely adopted in inves-

tigating counterflow gaseous flame structures and flame extinction conditions, with comparisons to experimental data obtained along the axis of symmetry. For low relative velocity of droplets with respect to the gas velocity, i.e., small-droplet Reynolds number, it can be assumed that the source terms S_m, $S_u/r \equiv S_l$, and S_h contributing to the gas-phase conservation equations are functions of axial coordinate x, as shown in Ref. [2] for outer potential flow and in Appendix A for rotational flow with plug flow boundary conditions. Here, S_m is the mass transfer per unit volume from the droplets to the gas, S_u the radial momentum transfer per unit volume from the droplets to the gas, and S_h the enthalpy transfer per unit volume from the droplets to the gas.

With these source terms, the conservation equations for mass, momentum in r direction, species, and energy can be cast in a quasi-one-dimensional form. These equations, together with the equation of state specifying the gas density, are listed below

$$\frac{d}{dx}(\rho v) + 2\rho U = S_m \tag{2}$$

$$\rho v \frac{dU}{dx} + \rho U^2 = -J + \frac{d}{dx}\left(\mu \frac{dU}{dx}\right)$$
$$+ S_l - U S_m \tag{3}$$

$$\rho v \frac{dY_k}{dx} + \frac{d}{dx}(\rho Y_k V_k) = W_k \dot{\omega}_k$$
$$+ (\delta_{ik} - Y_k)S_m,$$
$$k = 1, \ldots, N \tag{4}$$

$$\rho \sum_{k=1}^{N}(v + V_k)Y_k c_{p_k} \frac{dT}{dx} = \frac{d}{dx}\left(\lambda \frac{dT}{dx}\right)$$
$$- \sum_{k=1}^{N} W_k \dot{\omega}_k h_k + S_h$$
$$h_l S_m \tag{5}$$

$$\rho = \frac{p_0}{(R^0 \overline{W})T} \tag{6}$$

where ρ is the gas density, μ the gas viscosity, λ the gas thermal conductivity, $\dot{\omega}_k$ the molar

production by chemical reactions of species k, h_k the specific enthalpy of the species k, c_{pk} the specific heat at constant pressure of the species k, V_k the axial mass diffusion velocity of species k, W_k the molecular weight of species k, W the average gas molecular weight, R^o the universal constant of gases, i the index of the evaporating species, and δ_{ik} the Kronecker delta. The term $J = (1/r)(\partial p/\partial r)$ in Eq. 3 cannot be neglected as its limiting value at the x-axis is not zero and, in fact, is a constant [6, 12, 13].

The flow velocities, chemical compositions, temperature, and pressure at the nozzle exits are assumed given (as controllable or measurable quantities). Therefore, if x_l and x_u are the axial positions of the lower and upper nozzles shown in Fig. 1, the boundary conditions can be written as

$$v(x_l) = v_l, \quad v(x_u) = v_u$$

$$U(x_l) = U_l, \quad U(x_u) = U_u, \quad Y_k(x_l) = Y_{k_l},$$

$$Y_k(x_u) = Y_{k_u} \quad k = 1, \ldots, N$$

$$T(x_l) = T_l, \quad T(x_u) = T_u$$

$$p(x_l) = p(x_u) = p_0 \tag{7}$$

Unless otherwise mentioned, the values used here are $T_l = T_u = 300$ K, $p_0 = 1$ atm, $x_l = -0.4$ cm, $x_u = 0.6$ cm, and $U_u = U_l = 0$. The composition of fuel stream is pure methane, so that $Y_{CH_4,l} = 1$, but that of air can be different, depending on the water vapor or droplets used. The values of v_l and v_u are varied to get different flame extinction conditions. Because only the first derivative of v appear in the equation of mass, v cannot satisfy both the mass equations and the two B.C.'s. Thus, the term J acts as a constant pressure parameter, or an eigen value, that allows the mass equation to be satisfied, once v is specified at the boundaries. The solution of the system of equations described above is exact on the x-axis and is approximate for small values of r compared to the radius of the air nozzle. With the reduced number of discretized equations, finite-rate chemistry effects can be resolved accurately using a detailed reaction mechanism in a highly refined numerical grid along the axis of symmetry.

Singularities of Droplet Number Density Equation

The dynamics of a single droplet can be determined by integrating in time its equations of mass, momentum, and energy. Previous studies [2, 3] have suggested that condensed-phase effects can be coupled to the gas phase by simply multiplying the interaction of one droplet by the local droplet number density, n_d, that should satisfy a steady-state equation. However, in the case of the counterflow field, difficulties arise as droplets can penetrate the stagnation plane and reverse their trajectories [4]. If Eulerian formulation is used for droplets, with self-similarity formulation, the equation describing the conservation of droplet number density, n_d, can be written as (assuming droplets are not created or destroyed)

$$\frac{d}{dx}(n_d v_d) + 2n_d U_d = 0. \tag{8}$$

where $U_d = u_d/r_{d0}$, with v_d and u_d being the axial and radial velocity components of the droplet and r_{d0} the initial radial location of the droplet (very close to the axis of symmetry) at the air nozzle exit. The above equation assumes that, for any point in the domain where the equation is regular, n_d and U_d can be uniquely defined. Assuming U_d is assigned or already calculated from single droplet equations, the above equation indicates that dn_d/dx blows up as $v_d \to 0$, and therefore n_d.

Such a high peak in n_d is not expected in the droplet flow, where the average distance between droplets can vary from about 20 to 35 or more droplet diameters and their motion is quite ordered. In fact, n_d cannot even be strictly defined as the number of droplets per unit volume because the sample volumes are layers perpendicular to the x-axis and their thickness can be of the same order as the droplet diameter. Under such conditions, as the droplet motion cannot be treated as a continuum, the problem needs to be reformulated in a different way, i.e., by using a Lagrangian description of the droplet motion as described below.

Conservation Equations for the Condensed Phase

The Lagrangian equations that describe the conservation of mass, momentum, and enthalpy of a single droplet in a steady counterflow field are considered here. The droplet number density considered is small (corresponding to a maximum water mass fraction of 3% in condensed phase), so that the average distance between droplets is at least an order of magnitude greater than their diameters. Hence, droplet–droplet interactions, especially collisions, can be neglected. The droplet is assumed to be spherical and nonrotating. For simplicity, the temperature of the droplet is assumed to be uniform, but is allowed to vary in time from the room temperature at the nozzle exit to the equilibrium temperature determined by the heat transfer and evaporation rate (see Eq. 24).

To integrate such equations describing the droplet motion, simplified models are needed to describe the viscous forces through Stokes drag formulation and heat and mass transfer through Spalding's transfer number concepts (see Appendix A). The boundary conditions necessary for such lumped models are averaged gas velocities, temperature, water vapor mass fraction, and transport coefficients. All such variables are assumed to vary along the flow stream lines with characteristic lengths greater than the droplet diameter. Under such assumptions, a self-similar solution for the droplet dynamics can also be used. Introducing the subscript d to identify the conditions of the droplet, the appropriate dynamical variables characterizing the state of the droplet can be defined by velocity components v_d and U_d ($\equiv u_d/r_{d0}$), mass m_d (or diameter d, knowing the density of water, ρ_d), and temperature T_d. The resulting Lagrangian equations for mass, momentum, and energy to be solved are (see Appendix A for further details)

$$\frac{d}{dt}(d^2) = -\frac{8\bar{\lambda}\Psi}{\rho_d c_p} \tag{9}$$

$$\frac{dv_d}{dt} = \frac{18\bar{\mu}}{\rho_d d^2}(v - v_d) \tag{10}$$

$$\frac{dU_d}{dt} = -U_d^2 + \frac{18\bar{\mu}}{\rho_d d^2}(U - U_d) \tag{11}$$

$$\frac{dT_d}{dt} = \frac{12\bar{\lambda}}{\rho_d c_{p_d} d^2}\left[\frac{(T_\infty - T_d)\Psi}{\exp(\Psi) - 1} - \frac{L\Psi}{c_p}\right] \tag{12}$$

where Ψ is the Spalding's transfer number given by

$$\Psi = \frac{1}{Le_i}\ln\left(\frac{1 - Y_i}{1 - Y_{i_s}}\right) \tag{13}$$

The solution of the above equations yields the transfer of mass, momentum, and energy from a single droplet to the gas phase along the droplet trajectory until it is completely vaporized. The details of coupling the source terms arising from a single droplet to the source terms appearing in gas phase Eqs. 2–5 are described next.

Source Terms S_m, S_U, and S_h

In principle, the source terms S_m, S_U, and S_h contributing to the gas-phase equations can be determined by integrating Eq. 8 for the droplet number density, n_d, and then multiplying Q, $QU_d - F_r/r_d$, and $Q(h_d + L) - H$ (i.e., negative of the right-hand side of Eqs. A13, A15, and A16 by n_d at each location along the x-axis. As discussed earlier, the solution of such a Eulerian equation for n_d diverges if the droplet velocity approaches zero exactly at any node. Consequently, the source terms will also blow up when multiplied by n_d to include multiple droplets in the flow. Instead of integrating the droplet number density equation given by Eq. 8, if a Lagrangian equation for droplet flux is integrated in time, then the source terms contributing to equations for mass, momentum, and enthalpy will remain finite even at the droplet turning point. The development of an appropriate Lagrangian equation for droplet flux fraction is described below.

In Appendix A, it is shown that, under some simplifying but reasonable assumptions, m_d, v_d, U_d, and T_d are not functions of r_{d_0}, at least near the axis of symmetry. This means that droplets crossing the inlet section A_0 at the same time t_0 then cross section A_1 together, at time t_1, A_2 at time t_2, etc., with same m_d, v_d, U_d, and T_d as shown in Fig. 2. Taking advantage of this property, in the present calculation of source terms, a droplet *flux-fraction function* $\mathcal{F}(t)$ is introduced as the ratio between the number of
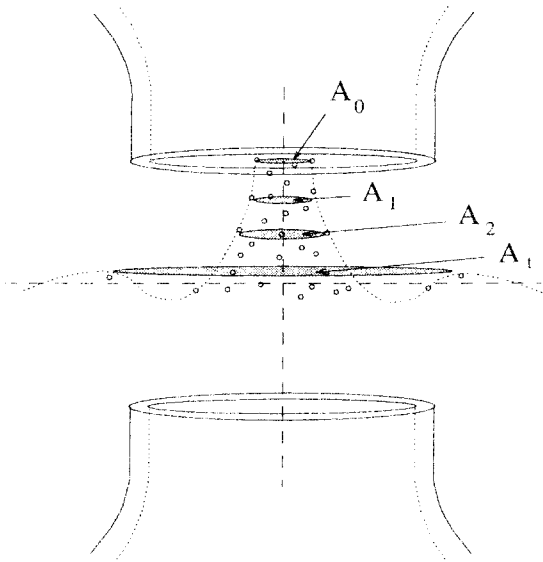
Fig. 2. An illustration showing the effect of flow strain on areas formed by water droplet streams as a function of time.

Fig. 3. An illustration of the axial motion of droplets in time, for two extreme droplet sizes.

droplets crossing a unit surface area perpendicular to the x-axis at time t and the number of droplets crossing an equivalent area at time t_0. Because of the self-similarity approximation, Eq. A12 shows that, if the droplets are uniformly distributed at time t_0, $\mathcal{F}(t)$ is independent from the radial distance r, as the distance from the x-axis of each droplet increases in time with the same factor $\mathcal{R}(t)$. Therefore, $\mathcal{F}(t)$ may be also defined as the ratio between A_0 and A_t, as all the droplets crossing A_0 also cross A_t, and their distribution remains uniform over each cross section. The number of droplets crossing section A_0 is $n_{d0}v_{d0}$. It is only near the turning point that a droplet number density cannot be satisfactorily defined. Therefore, the number of droplets crossing a unitary surface perpendicular to the x-axis at time t is $n_{d0}v_{d0}\mathcal{F}(t)$. By considering a differential volume, in the limit time step $dt \rightarrow 0$, it can be shown that the function $\mathcal{F}$ satisfies the following equation

$$\frac{d\mathcal{F}}{dt} = -2\mathcal{F}U_d \tag{14}$$

(Note: the above equation can also be obtained by integrating Eq. 11 to find A_t.) At time t_0, $\mathcal{F} = 1$ by definition. Once the equations for a single droplet, described by Eqs. 9–12 and 14, are integrated in time, values of m_d, U_d, h_d, and
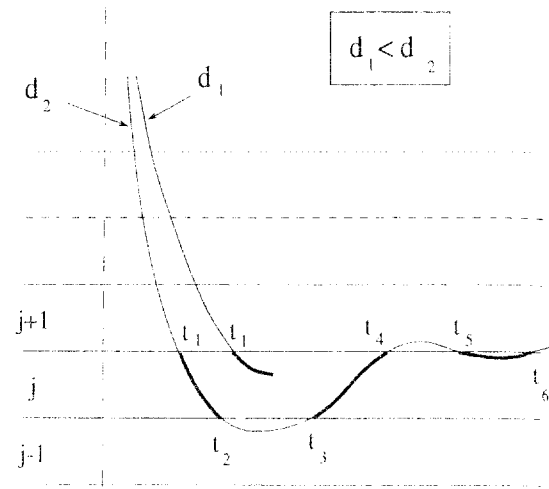
$\mathcal{F}$ are known along the entire droplet path, i.e., from the point on A_0 to complete evaporation. This information is next used to determine the source terms contributing to each node in Eulerian formulation of the gas-phase equations.

Consider the case where the counterflow region is divided into fixed layers whose thickness is at least a few times larger than the droplet diameter. As illustrated in Fig. 3, a droplet may cross the boundaries of any volume dV_j a few times or go to complete vaporization in this volume element. Such phenomena are very likely to happen if the volume dV_j is close to the stagnation plane. Each droplet that moves inside dV_j transfers mass, momentum, and enthalpy to the gas in a time interval dt by the amount

$$\delta_j\phi = -\phi(t)dt \tag{15}$$

where ϕ represents the right-hand side terms in Eqs. A13, A15, and A16 (i.e., $-Q$, $-QU_d + 3\pi d\bar{\mu}(U - U_d)$ and $-Q(h_d + L) + H$). Because the number of droplets that cross the plane A_0 per unit area per unit time is $n_{d0}v_{d0}$, the number of droplets reaching the element dV_j and contributing to Eq. 15 per unit area and unit time is $n_{d0}v_{d0}\mathcal{F}(t)$. Assuming that the path of each droplet in dV_j is divided into intervals $\{t_k, t_k + dt_k\}$, $k = 1, \ldots, K_j$, the mass, momentum, and enthalpy transfer in the volume $dx_j dA$ are given by

$$\Delta_{k}\phi = -\left[n_{d}Y_{k} \sum_{k=1}^{K} \int_{t_{i}}^{t_{i}+dt} \dot{m}(t)\phi dt \right] dA \tag{16}$$

In terms of per unit volume, as in Eqs. 2–5. Eq. 16 can be written as

$$S_{\phi} = -(1/dx_{j}) n_{d} Y_{k} \sum_{k=1}^{K} \int_{t_{i}}^{t_{i}+dt} \dot{m}(t)\phi dt \tag{17}$$

In Eq. 17, the droplet mass center is assumed to be in dV_{j}. For finite sized droplets, when their mass centers are near the boundary of dV_{j}, part of the droplet surface is in the adjacent volume, so that the contributions to the source terms should be shared accordingly. However, the correction to Eq. 17 may be considered negligibly small in case the droplet has a diameter much smaller than dx, or the source term contributions vary only slightly in a distance of the order of the droplet diameter. In case the latter condition is not satisfied, the lumped description of the gas–droplet interaction described in this work is not possible.

It should be pointed out that, in the present formulation, the droplets leaving the air nozzle are assumed be monodisperse. In actual experiments, achieving a monodisperse droplet loading is a challenging task. Although experiments with water droplets have not been performed yet at the present time, some droplet diameter distribution is expected around a mean value. The formulation described above, however, can be easily generalized by approximating such a continuous distribution of droplets as a collection of discrete sections with average droplet diameters d_{l} ($l = 1, L$). The single droplet equations then can be solved, and Eq. 17 can be evaluated for each section d_{l} by replacing n_{d} with $f_{l}n_{d}$, where f_{l} is the fraction of droplets having diameter d_{l}. In the present study, the above generalization is not undertaken until the experimental results become available.

NUMERICAL APPROACH

Integration of Gas-Phase Equations

Equations 2–5 describe a set of nonlinear ordinary differential equations for $N + 4$ unknowns, namely, T, $Y_{k}(k = 1, \dots, N)$, U, v, and J. Numerical methods have been used in the past to obtain accurate solutions for the system of equations, without the source terms S_{m}, S_{U}, and S_{h} [15–17]. These involve use of first-order finite difference methods with pseudo-Newton algorithm steps. Although other higher-order methods are available, the method used is unconditionally stable and requires just a three-point stencil. Unconditional stability is of paramount importance in the solution of chemically reacting gases, where the presence of sharp variations in mass fraction profiles may lead to nonphysical solutions or no convergence at all. The three-point stencil simplifies the inversion of the Jacobian in the pseudo-Newton steps, as the matrix turns out to be a block tridiagonal, for which stable solution codes are available. Convection terms are approximated with an upwind scheme. In particular, in calculating the enthalpy transport in Eq. 5, the upwind scheme is applied using the total mass average velocity of each species k, by $v + V_{k}$. Adaptive grid refinement is also performed after the solution converges. This allows the first-order method to yield accurate results without using too many grid points. For cases where uniform grids are used, typical grid spacing is about $\Delta x_{j} = 10 \ \mu m$.

In solving Eqs. 2–5, the thermochemical and transport properties, namely, ρ, H_{k}, X_{k}, $\bar{\omega}_{k}$, c_{p}, h_{k}, $D_{k}(k = 1, \dots, N)$, λ, and μ, are calculated at each point x_{j} using the Chemkin and transport libraries [18, 19]. The chemical reaction rates are modeled by 17 species in 30 elementary reaction steps [20]. For low Mach number flow considered here, pressure p_{0} is assumed given. Integration of droplet equations and determination of the source terms S_{m}, S_{U}, and S_{h} are discussed below.

Integration of Droplet Equations

The single droplet equations must be solved at the end of each pseudo-Newton step to update the source terms S_{m}, S_{U}, and S_{h} contributing to Eqs. 2–5. These are performed at every iteration step so that no droplet property needs to be stored. The algorithm used for their solution must be (1) accurate enough to produce error not greater than the modeling itself, (2) fast

enough to allow analysis of different flow conditions in a reasonable time and (3) most of all robust, as the equations must be solved for droplets of different sizes and different flow field conditions. Because the variables controlling droplet equations vary slowly in space as compared to some radical species or chemical reaction rates, in the procedure employed here, a new set of coarse grid points $x_{sj}(j = 1, \ldots, N_x + 1)$ is used for the integration of droplet equations. To analyze the grid independence of the solution, the coarse grid chosen consists of equidistant points at intervals Δx_s greater by some factor than the initial droplet diameter. On the selected coarse grid points, the values of v, Y_k, U, and T are linearly interpolated. To be consistent, these values are then used to determine the gas-phase properties using the Chemkin and transport libraries [18, 19] as well as liquid and liquid–vapor equilibrium properties from thermodynamic table data [21].

The integration time step is chosen each time so that the droplet will not travel more than a fraction of the coarse grid interval. Denoting each quantity calculated at time t_n with the superscript n, and at time $t_{n+1} = t_n + \delta t_n$ with the superscript $n + 1$, the single droplet equations are approximated in the following form:

$$\frac{(d^2)^{n+1} - (d^2)^n}{\delta t_n} = -\frac{8\bar{\lambda}^n \Psi^n}{\rho_d c_p^n} \tag{18}$$

$$\frac{v_d^{n+1} - v_d^n}{\delta t_n} = \frac{18\bar{\mu}^n}{\rho_d (d^2)^n}(v^n - v_d^{n+1}) \tag{19}$$

$$\frac{U_d^{n+1} - U_d^n}{\delta t_n} = -U_d^n U_d^{n+1} + \frac{18\bar{\mu}^n}{\rho_d (d^2)^n}$$
$$\cdot (U^n - U_d^{n+1}) \tag{20}$$

$$\frac{T_d^{n+1} - T_d^n}{\delta t_n} = \frac{12\bar{\lambda}^n}{\rho_d c_{p_l}(d^2)^n}$$
$$\cdot \left[\frac{(T_\infty^n - T_d^n)\Psi^n}{1 - \exp(\Psi^n)} - \frac{L^n \Psi^n}{\bar{c}_p^n} \right] \tag{21}$$

$$\frac{x_d^{n+1} - x_d^n}{\delta t_n} = 0.5(v_d^n + v_d^{n+1}) \tag{22}$$

$$\frac{\mathcal{F}^{n+1} - \mathcal{F}^n}{\delta t_n} = -\mathcal{F}^{n+1}(U_d^n + U_d^{n+1}) \tag{23}$$

The gas-phase properties appearing in these equations are calculated only at time t_n, including v and U, as implicit schemes can be very time consuming. The terms in the right-hand side of Eqs. 18–23 could be calculated at time t_n, yielding a simple explicit, first-order method. However, nonphysical oscillations might appear in v_d, U_d, and $\mathcal{F}$ (the instability of T_d is discussed separately below) in case δt_n is not small enough, which is the case when m_d approaches zero (or $d^2 \rightarrow 0$).

To improve the stability of the ordinary differential equation (ODE) solver, v_d, U_d, and $\mathcal{F}$ appearing on the right-hand sides of Eqs. 18–23 are evaluated at time t_{n+1}, with the exception of the term U_d^2, which is not fully implicit, i.e., $U_d^n U_d^{n+1}$ instead of $(U_d^{n+1})^2$, to keep the equation in U_d^{n+1} linear. Also v_d and U_d in Eqs. 22 and 23 appear as averages between values at t_n and t_{n+1} to improve the accuracy. The method used in Eqs. 18–23, although not fully explicit or fully implicit, is consistent (converges to the ODE as $\delta t_n \rightarrow 0$), first order, and absolutely stable. The error introduced can be made arbitrarily small by reducing δt_n until it becomes smaller than the error introduced calculating the source terms on the coarse uniform grid $x_{sj}(j = 1, \ldots, N_x + 1)$ instead of on the original grid $x_j(j = 1, \ldots, N_p + 1)$ where the Eulerian equations are discretized.

As the droplet enters the hot mixing layer, its temperature increases rapidly, and the numerical approximation for T_d^{n+1} can overshoot the value determined by the thermal equilibrium, i.e., balance between the heat transfer to the droplet and heat of evaporation. This equilibrium temperature of the droplet, $T_{d\epsilon}^n$, where these two terms balance is given by

$$(T_\infty^n - T_{d\epsilon}^n) = \frac{L^n}{\bar{c}_p^n}(1 - \exp(\Psi^n)) \tag{24}$$

To eliminate spurious oscillations associated with overshoots of droplet temperature, when T_d^{n+1} given by Eq. 21 is greater than $T_{d\epsilon}$, the condition $T_d^{n+1} = T_{d\epsilon}^n$ is imposed. This essentially implies that, as the characteristic time of T_d becomes much smaller than δt_n, the asymptotic solution of thermal equilibrium is justifiable and is used here.

Calculation of Source Terms

Once d, v_d, U_d, T_d, and $\mathcal{F}$ are determined from Eqs. 18–23, the source terms are first calculated from Eq. 17 at the coarse and uniform grid points x_{sj}. If both the droplet locations x_d^n and points x_{sj} (given by Eq. 22) are in the same Δx_s, x_d^{n+1} (given by Eq. 22) are in the same Δx_s, centered in x_{sj} (i.e., the droplet center of mass remains in the same volume), then all the contributions are assigned to the point x_{sj}, while on all the other points x_{sk} ($k \neq j$) the source terms are not modified. Alternatively, x_d^{n+1} must be in the volume centered in one of x_{sj}'s two neighbors because of the small time steps taken. In the latter case, the contributions to the source terms are then shared by the two grid points proportionately based on the fraction of time δt_n spent by the droplet in each of the corresponding volumes. Subsequently, the values of S_{mj}, S_{Uj}, and S_{hj} used at the points x_j ($j = 1, \ldots, N_p + 1$) in the Eulerian formulation are calculated interpolating from the values given above.

The numerical approximations introduced above in evaluating the terms S_{mj}, S_{Uj}, and S_{hj} certainly can have some errors associated with them. For example, the first-order temporal integration scheme using the values of gas-phase properties interpolated on a coarse grid can be a source for such errors. However, the procedure adopted here gives acceptable numerical results when the gas-phase properties that affect the droplet dynamics change on a scale equal to or greater than Δx_s, and the time step δt_n is taken small enough. Also, when a droplet is crossing the boundary between two volumes, the contributions that are not more rigorously given to one of the volumes when droplet mass center is, in fact, located in the adjacent cell can be another source of an error. Such errors are however minimized by taking small time steps. Because a rigorous analysis of the error is not possible due to the nonlinearity of the problem, an attempt to quantify the errors associated with the hypothesis introduced, by using a sensitivity analysis, is discussed later in the paper.

Solution Algorithm

The equations describing the gas phase with the droplet source terms can be written in the form

$$F(\mathbf{s}, \mathbf{S}) = 0 \tag{25}$$

where $\mathbf{s}$ represents the matrix $s_{i,j}$ ($i = 1, \ldots, N + 4$, $j = 1, \ldots, N_p + 1$) of the $(N + 4) \times (N_p + 1)$ unknowns T_j, Y_{kj}, ($k = 1, \ldots, N$), U_j, v_j, and J_j, ($j = 1, \ldots, N_p + 1$) and $\mathbf{S}$ the vector of the source terms S_{mj}, S_{Uj}, and S_{hj}, ($j = 1, \ldots, N_p + 1$). With a "good" initial guess for $\mathbf{s}$, these equations are integrated with an algorithm that uses quasi–Newton steps. After $n + 1$ steps, the approximation of the solution is given by

$$\mathbf{s}^{n+1} = \mathbf{s}^n - (J|_s^{-1})^n F(\mathbf{s}^n, (1 - \gamma)\mathbf{S}^n + \gamma \mathbf{S}^{n+1}) \tag{26}$$

where $\mathbf{s}^n$ and $\mathbf{S}^n$ are the solution and droplet source terms $\mathbf{S}$ after n steps, respectively, and $(J|_s^{-1})^n$ is the inverse of the Jacobian calculated at step n keeping the source terms constant. The Jacobian is in block-tridiagonal form and is calculated numerically and then inverted, calling a subroutine already used in previous work [15–17]. Here, a relaxation parameter $\gamma < 1$ is introduced to speed up the convergence to steady-state solution.

As shown in Eq. 17, the source terms depend on the gas-phase values at the points that are used to integrate the single droplet equations. However, such dependence is not accounted in the Jacobian, otherwise, the matrix would lose its property of being block tridiagonal. This means that $J|_s$ is only an approximation of the real and less-sparse Jacobian. In general, convergence is quite fast (no more than five or six iterations), but it can become a problem when S_{mj}, S_{Uj}, and S_{hj} peak values are large or become very sensitive to the solution. For this reason, in Eq. 26, F is sometimes calculated introducing the relaxation factor γ with $\mathbf{S}^{n+1}$, to compensate for very quick variation of S_{mj}, S_{Uj}, and S_{hj} at each step.

The solution is assumed to have converged when

$$\frac{\|\bar{\mathbf{s}}^{n+1} - \bar{\mathbf{s}}^n\|}{(N + 4)(N_p + 1)} \leq \epsilon_0 \tag{27}$$

where $\bar{\mathbf{s}}$ is the vector of the unknowns scaled by some reference value of the solution variables, and ϵ_0 is a small prefixed value. If the solution converges, a grid refinement step is performed
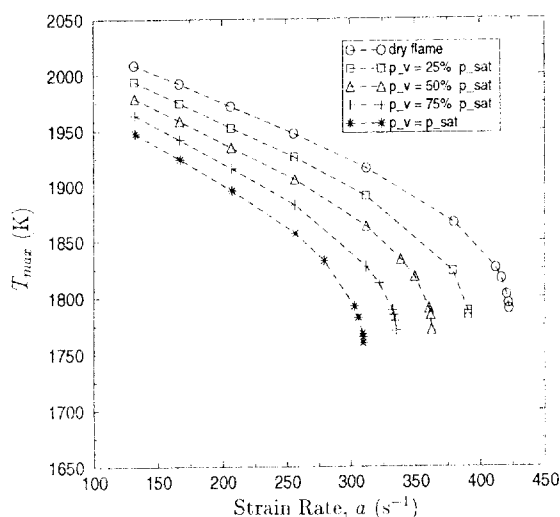
Fig. 4. Comparison of the maximum flame temperature. T_{max}, vs. flow strain rate, a, for different inflow water vapor partial pressures.

to determine whether and where new grid points must be added based on the evaluated gradients and curvatures, and the iteration process is repeated [17].

EFFECT OF WATER VAPOR ON FLAME EXTINCTION

In a real-life fire situation, or in laboratory experiments, when water droplets are introduced to suppress flames, they are bound to saturate the room air with water vapor. Consequently, the fraction of oxygen displaced (or diluted) by the water vapor can reduce the flame strength, or the extinction strain rate (a_{ext}), of the counterflow flame considered here. Figure 4, for example, shows a comparison of the predicted variation of maximum flame temperature, T_{max}, as a function of the flow strain rate (a), for some selected water vapor concentrations. The line with symbol $\bigcirc$ corresponds to a dry case, whereas the symbol * correspond to a fully saturated case at a room temperature of 300 K and atmospheric pressure (i.e., partial pressure of water $p_{H_2O,sat} = 0.0351$ atm or, in mass fractions, $Y_{H_2O,a} = 0.0222$, with $Y_{O,a} = 0.2278$ and $Y_{N,a} = 0.7500$). The fuel considered in these calculations is pure methane ($Y_{CH_4,f} = 1.0$). Based on this figure, if the

asymptotic value of highest strain rate for each case is taken as the extinction strain rate, a_{ext}, then the results indicate that saturated water vapor alone can decrease the flame extinction strain rate by 25%. This enhanced effect is not solely due to dilution, but is partly due to the high thermal capacity of water.

DYNAMICS OF WATER DROPLETS WITHOUT INTERACTION

If the amount of water being injected into the air stream is greater than $p_{H_2O,sat} = 0.0351$ atm (or $Y_{H_2O} > 0.0222$), then the excess water will be in condensed form, i.e., in the form of droplets. The mass fraction of water associated with such droplets leaving the air nozzle can be defined using

$$Y_0 = \frac{m_{d0} n_{d0} v_{d0}}{m_{d0} n_{d0} v_{d0} + \rho_a v_a} \tag{28}$$

where m_{d0} is the initial mass of the droplet, n_{d0} the initial number density, v_{d0} the initial velocity of the droplet, and ρ_a and v_a are the density and velocity of air leaving the nozzle, respectively. All the results shown here are obtained by assuming that the droplet velocity leaving the air nozzle is same as that of the gas, i.e., $v_{d0} = v_a$, but other inflow conditions can be easily analyzed with the model developed. One of the major objectives of the present work is to understand the trajectories of condensed-phase, monodisperse water droplets in a reacting counterflow field considered here and investigate their effect on the flame extinction condition.

In the present predictions, the effect of various monodisperse droplet sizes for three different fixed water mass fraction in the condensed phase ($Y_0 = 1$, 2, and 3%) is considered, to make fair comparisons. Table 1 shows the number density of water droplets leaving the air nozzle, n_0 (#/cm³), for three different Y_0 and for three different monodisperse droplet sizes selected. The last column in Table 1 also lists the characteristic separation length between droplets, l_0 (cm). It is interesting to note that, for all the combinations of water mass fraction in condensed phase and droplet sizes, the ratio of droplet separation length to the droplet diameter, l_0/d, remains fairly large (>20) and is

TABLE 1

Comparison of the Number Density and Droplet Separation Lengths for Some Selected Water Mass Loadings

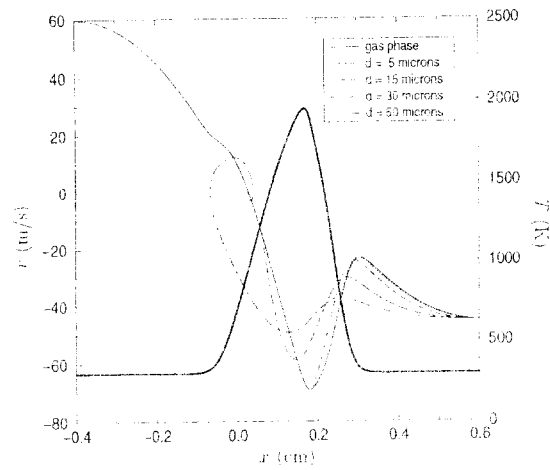| Y_0	d (μm)	n_0 (cm^{-3})	$n_0^{1/3}$ (cm^{-1})	l_0 (cm)
1% $l/d = 35$	5	178408	56.3	0.0177
	20	2787	14.1	0.0711
	50	178	5.6	0.1778
2% $l/d = 28$	5	360457	71.2	0.0141
	20	5632	17.8	0.0562
	50	360	7.1	0.1406
3% $l/d = 24$	5	546259	81.7	0.0122
	20	8535	20.4	0.0485
	50	546	8.2	0.1223

Fig. 5. Comparison of the gas velocity and droplet velocity of different sizes, with droplet source terms turned "off" in gas-phase calculations. Also shown is the gas temperature (thick line).

of the same order. This implies that the neglect of droplet–droplet interaction is reasonable for all the cases considered here. It should be pointed out that in actual water-mist systems, it is highly unlikely that the water droplets generated are monodisperse. However, under very low water mass flow rates, the generation of monodisperse water droplets in laboratory experiments is well established and is being pursued by several groups, including our group at the University of Virginia. The predictions performed here with monodisperse droplets provides a better mechanism to analyze and understand the basic droplet dynamics and interactions with the gas-phase processes, which can be easily extended to polydisperse droplet flows in the future.

As mentioned previously for dilutely loaded droplets, the gas displacement by water droplets can be neglected because of the large density ratio between the condensed water and the gas. Under such conditions, the only interaction between the droplets and the gas is because of the source terms S_m, S_r, and S_h appearing in Eqs. 2–5. When these terms are included in the numerical calculations, the flame structure and extinction strain rate are affected dramatically, depending on the amount of condensed water added and the droplet sizes. Thus, for the purpose of illustrating and comparing the trajectories of various droplet sizes in the counterflow field and their associated source terms, a fixed low-strain rate case ($a = 130$ s^{-1}) where the droplet source terms are excluded (or the source terms turned "off" in numerics) is con-

sidered first. It should be mentioned here that the profiles of droplet trajectories and source terms presented below remain essentially the same for high-strain rates as well. Figure 5 shows a comparison of the axial velocity along the axis of symmetry of the gas and droplets of different sizes for the selected low-strain rate case. Although the coupling arising from the droplet source terms on gas-phase structure is neglected, in solving droplet equations for droplet trajectory shown in Fig. 5, the droplet vaporization effects are included in Eqs. 18–23. In Fig. 5, the 5-μm droplets are seen to follow the gas fairly closely, whereas large droplets deviate considerably. The droplet lag seen becomes slightly worse for high-strain rates, especially near extinction conditions. The 5-μm droplets are also seen to be completely vaporized soon after they enter the hot mixing layer, whereas 50-μm droplets penetrate through the flame and also the stagnation plane and then reverse their direction somewhere in the fuel stream. If the droplet vaporization is suppressed, then the penetration of 50-μm droplets is much more pronounced, with multiple crossings at the stagnation plane. These predictions are consistent with those reported earlier by Chen et al. [4].

The droplet response to the variation in gas-phase flow conditions can be characterized by the Stokes number, St. By defining the flow residence time in the outer air flow as $t_f = 1/a$,

TABLE 2

Comparison of the Stokes Number (St) for Different Droplet Sizes for $a = 130$ s^{-1}

d (μm)	t_d (s^{-1})	t_{ta} (s^{-1})	St
5	0.7523×10^{-4}	0.7633×10^{-2}	0.0098
10	0.3009×10^{-3}	0.7633×10^{-2}	0.0394
15	0.6770×10^{-3}	0.7633×10^{-2}	0.0887
20	0.1204×10^{-2}	0.7633×10^{-2}	0.1577
25	0.1881×10^{-2}	0.7633×10^{-2}	0.2464
30	0.2708×10^{-2}	0.7633×10^{-2}	0.3548
40	0.4814×10^{-2}	0.7633×10^{-2}	0.6307
50	0.7523×10^{-2}	0.7633×10^{-2}	0.9855
60	0.1083×10^{-1}	0.7633×10^{-2}	1.4191

Fig. 7. Comparison of droplet temperature, T_d, of different droplet sizes, with droplet source terms turned "off" in gas-phase calculations. Also shown is the gas temperature (thick line).

and deriving an expression for the droplet response time (t_d) based on Stokes drag, the following expression can be derived for St

$$St = \frac{1}{a}\frac{18\mu}{\rho_d d^2} \qquad (29)$$

For the strain rate of 130 s^{-1} considered in Fig. 5, the variation of St for different droplet sizes in the outer oxidizer flow is shown in Table 2. It is seen that 5-μm droplets have truly small St number, consistent with the results shown in Fig. 5. As the droplet size approaches about 15 μm, the St number approaches about 0.1, indicating slower response of the droplet to the gas, as seen in Fig. 5.
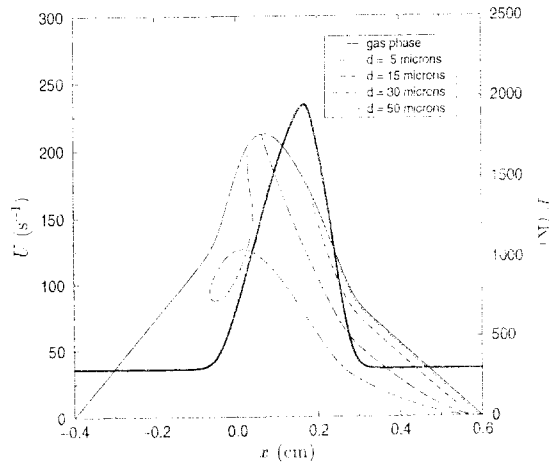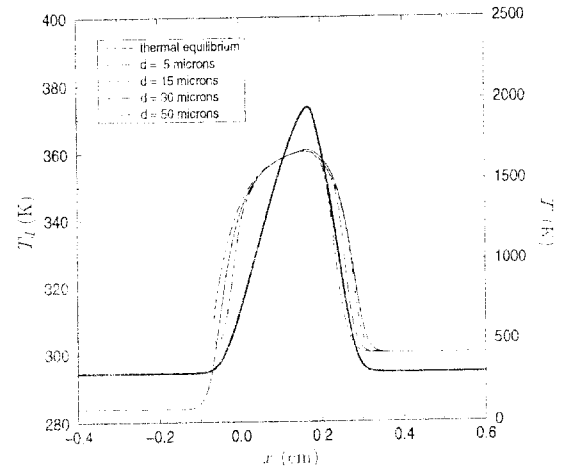
Figures 6–8 show the variation of other vari-

ables associated with the droplet, evaluated from Eqs. 20, 21, and 23, along the axis of symmetry. These results are again obtained under the same conditions as in Fig. 5. Figure 6, for example, shows that U_d is always less than U, which is expected, as the gas is accelerating radially from the axis of symmetry and is consistent with experimental measurements of methanol droplets in a counterflow by Li et al. [5]. Figure 7 shows that the temperature of 5-μm droplets (T_d) follows that obtained as-
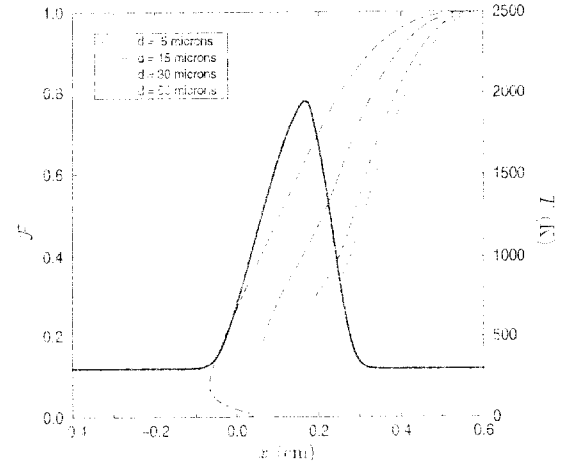
Fig. 6. Comparison of U of gas and U_d of different droplet sizes, with droplet source terms turned "off" in gas-phase calculations. Also shown is the gas temperature (thick line).

Fig. 8. Comparison of flux-fraction function, $\mathcal{F}$, of different droplet sizes, with droplet source terms turned "off" in gas-phase calculations. Also shown is the gas temperature (thick line).

suming thermal equilibrium condition given by Eq. 24 (solid line), whereas other droplets show a small thermal lag. However, this lag has insignificant effect on the flame structure and extinction condition considering the small temperature difference and the energy associated with it. The variation of flux fraction $\mathcal{F}$ as a function of the axial location, shown in Fig. 8, however, has a very important role on the droplet source terms described by Eq. 17, therefore, the state of the flame. The reduction in $\mathcal{F}$ seen as the droplet approaches the stagnation plane is because of the flow divergence or straining effect. If the droplet vaporization is neglected, the curves shown for different droplet sizes shift somewhat, but the dramatic reduction of $\mathcal{F}$ seen with droplet location does not change. Similar results for axial liquid methanol volume flux were observed experimentally by Li et al. [5], with and without a flame.

SOURCE TERMS WITHOUT INTERACTION

Once the solution of droplet variables is obtained (i.e., d, v_d, U_d, T_d, and $\mathcal{F}$), the source terms contributing to the gas phase can be evaluated through Eq. 17. Here, such contributions are shown, once again by turning "off" the interaction of such source terms with the gas-phase calculations to keep the flame structure condition the same for different droplet sizes considered.

Figures 9–11 show the variation of mass, momentum, and energy source terms, i.e., S_m, $S_L = US_m$, and $S_h = h_fS_m$, along the axis of symmetry for different droplet sizes. Figure 9 shows rather strange profiles, especially on the air side before the flame, where evaporation effects are negligible. It is seen that smaller droplets exert a greater radial force per unit volume on the gas than larger droplets. This is however easily explained by the fact that larger droplets shoot through that region faster than smaller droplets, so that they have much shorter residence time. A comparison of Figs. 10 and 11 indicates the profiles of S_m and $S_h = h_fS_m$ to be very similar (except for the change of the sign). This suggests that heat transfer to the droplets and evaporation are well correlated; the impli-
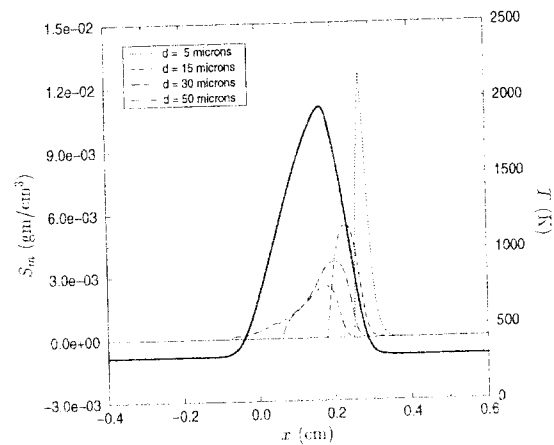

Fig. 9. Typical S_m profiles of different droplet sizes, with $Y_0 = 0.02$ and droplet source terms turned "off" in gas-phase calculations. Also shown is the gas temperature (thick line).

cations of such correlations are discussed further in the next section.

EFFECT OF WATER DROPLETS ON FLAME EXTINCTION

The most interesting question that can be probed by the two-phase model developed here is the effect of water droplets on flame extinction condition, when the source terms are included in the gas-phase solution, in particular, the role of water droplet size on the flame extinction condition for a given mass loading.
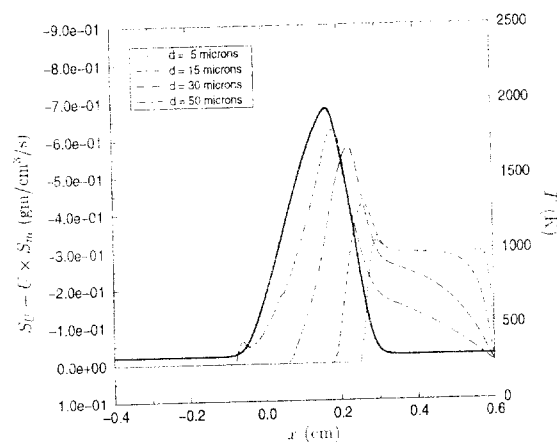

Fig. 10. Typical $S_L = US_m$ profiles of different droplet sizes, with $Y_0 = 0.02$ and droplet source terms turned "off" in gas-phase calculations. Also shown is the gas temperature (thick line).
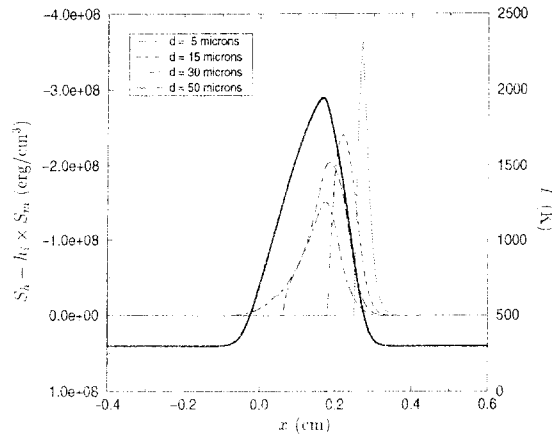
Fig. 11. Typical $S_h - h_i S_m$ profiles of different droplet sizes, with $Y_0 = 0.02$ and droplet source terms turned "off" in gas-phase calculations. Also shown is the gas temperature (thick line).

Such effects can be shown by plotting the variation of maximum flame temperature as a function of the flow strain rate, as shown in Fig. 12, similar to that shown earlier in Fig. 4 for water vapor effect. In addition to the saturated water vapor at room conditions (solid line), when condensed water 1% by mass is introduced, i.e., $Y_0 = 0.01$, in the form of different droplet sizes, different profiles for T_{max} are obtained and are plotted in Fig. 12 for comparison. This figure indicates that 50-μm droplets are the least effective with a relatively higher extinction
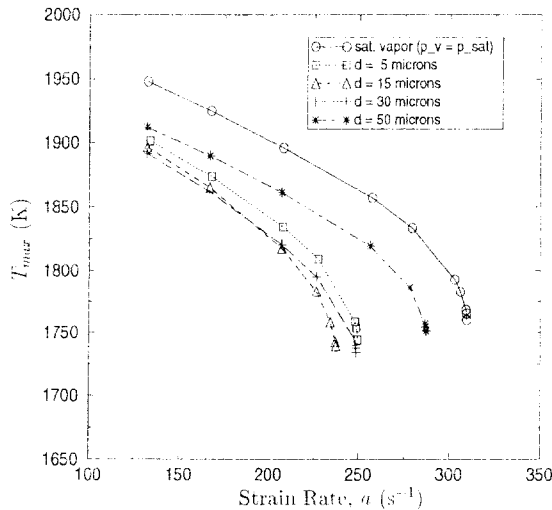

Fig. 12. Comparison of T_{max} vs. a, for different droplet sizes, with $Y_0 = 0.01$.
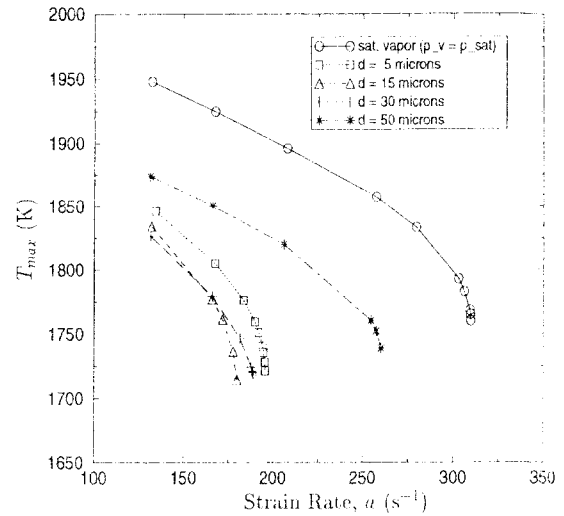

Fig. 13. Comparison of T_{max} vs. a, for different droplet sizes, with $Y_0 = 0.02$.

strain rate (still below the saturated vapor case with water vapor mass fraction of 0.022), while 15-μm droplets are the most effective with the lowest extinction strain rate. As the size of monodisperse droplets is decreased below 15 μm, they are seen to be less effective. The lowest size considered here is 5 μm, as the mass and enthalpy source terms approach a δ-function as seen in Figs. 9 and 11, introducing severe convergence problems of the numerical model. In fact, droplets of 5 μm and below should approach the limit where all the water considered is in vapor phase at the air side boundary of the mixing layer, provided the inflow temperature of air is not affected. Irrespective of this difficulty, the most interesting nonmonotonic behavior on droplet size is captured well by the two-phase model developed here for steady, laminar, counterflow, nonpremixed flames.

For higher water mass fractions in condensed phase, similar profiles for T_{max} as a function of flow strain rate are obtained, as shown in Figs. 13 and 14. However, the extinction strain rate is seen to reduce significantly with increasing water droplet loading. For various mass fractions considered here, the nonmonotonic effect of droplet size on the extinction strain can be better illustrated as shown in Fig. 15. For all the conditions considered here, 15- to 20-μm droplets are seen to be the most effective. This superior effectiveness of 15- to 20-μm droplets
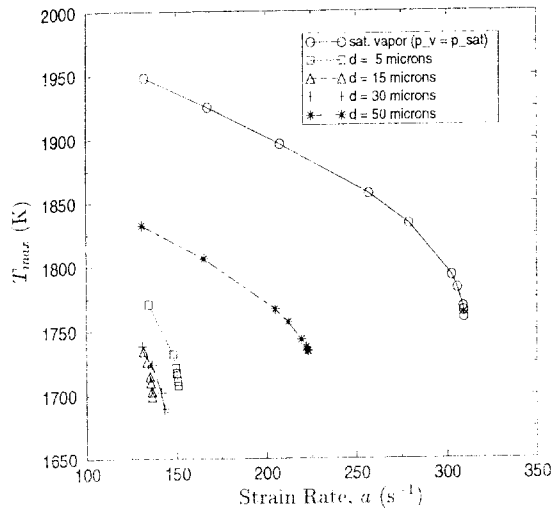
Fig. 14. Comparison of T_{max} vs. a, for different droplet sizes, with $Y_0 = 0.03$.

Fig. 16. Comparison of $(\chi_s)_{ext}$ vs. droplet size, for different droplet mass fractions in condensed phase at inflow.

can be explained by the location of the mass source term seen in Fig. 9. In the case of 15-μm droplets, the peak value of S_m, and also $S_h = h_f S_m$, is seen to occur at the oxygen consumption or radical production layer. The negative effect of $S_h = h_f S_m$ on flame temperature can result in lower radical production and hence early flame extinction [22, 23]. The exact physical, thermal, and chemical contributions responsible for flame extinction condition in the presence of water droplets are currently being
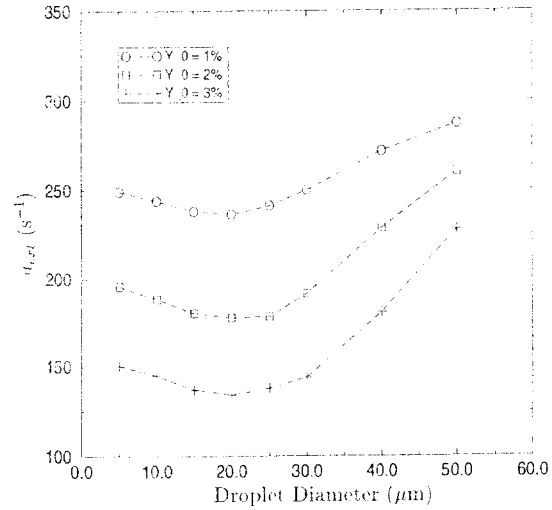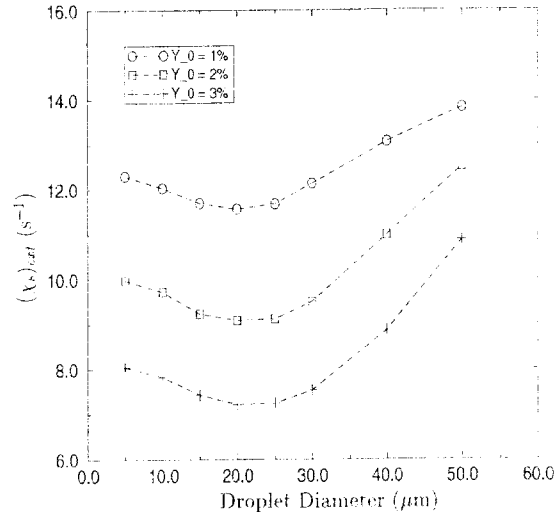
investigated separately, with comparison to that of traditional chemical agents, such as halon 1301.

The concept of flow strain rate as defined here, i.e., $a = -dv/dx$, is strictly applicable to constant density or nonreactive mixing layer flows. However, it is a useful fluid dynamical parameter for comparison with near extinction experimental velocity data obtained with nonintrusive laser-Doppler velocimetry techniques [6]. For theoretical studies, a more useful fluid dynamical parameter is the diffusion time scale defined by the inverse of the scalar dissipation rate [23, 24]

$$\chi = 2D|\nabla Z|^2 \tag{30}$$

where D is an appropriate diffusion coefficient (e.g., $D = \lambda/(\rho c_p)$ for unity Lewis number) and Z is the mixture fraction. For small stoichiometric mixture fractions, Z_s, an analytical expression relating the stoichiometric scalar dissipation rate, χ_s, with a taking into account the thermal expansion effects, has been derived by Kim and Williams [25]. Instead of using such an analytical expression, the scalar dissipation rate at the stoichiometric point at extinction is directly computed here by solving for a conservation equation for mixture fraction. The resulting variation of $(\chi_s)_{ext}$ as a function of the initial droplet size and water mass fraction in condensed phase is shown in Fig. 16, indi-

Fig. 15. Comparison of a_{ext} vs. droplet size, for different droplet mass fractions in condensed phase at inflow.

cating a trend similar to that of a_{ext} shown in Fig. 15.

The results presented here need to be validated with careful experimentation, and such studies are currently under way. However, the generation of truly monodisperse droplets is a challenging task, and methods of extending the present work to polydisperse droplets need to be pursued in the future.

SENSITIVITY OF THE RESULTS TO THE APPROXIMATIONS INTRODUCED

Several simplifications and approximations were used in the development of an analytical model for droplet equations. The implication of some of these approximations introduced and possible inaccuracies arising from these approximations are addressed here separately.

Grid and Time Step Size

In solving the set of ODE's described by Eqs. 2–5, an initial solution on a coarser grid is traditionally used, with subsequent refinements of the grid where the gradients and curvature are large. This method works well when the outer flow is approximated by a potential flow field where U is independent of x in the outer frozen flow region [16, 17]. However, for the rotational flow field used here, with plug flow boundary conditions, the grid refinement scheme does not add additional points to refine the outer flow region where the velocity gradient changes with x. To obtain accurate solution for the flow strain rate, a, based on the velocity gradient of the outer flow in the oxidizer side, the domain outside the mixing layer is artificially refined until the strain rate solution became independent of the grid selected. As mentioned previously, the droplet equations are solved on a coarser grid x_{sj} such that Δx_s is at least two times the largest droplet size considered, i.e., 100 μm. However, the final solution is found to be invariant with the coarser grid selection as long as the source terms contributing to each cell are appropriately partitioned, depending on the time spent on each cell. In addition to the grid selections, tests performed with the Lagrangian time step modified with a
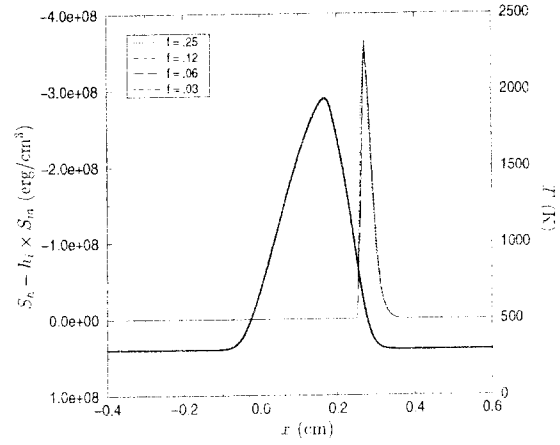
factor f are shown in Fig. 17. This figure indicates no change in the flame structure and very minor changes in S_m with the f values selected.

Quasi-Steady Droplet Evaporation and Heat Transfer Model

The expressions for Q and H described in Appendix A are derived under the assumptions that T_d is uniform in the droplet and that the quasisteady-state solutions of the surrounding gas can accurately approximate the water vapor concentration and temperature profiles. The above relies on the hypothesis that the characteristic times of mass diffusion τ_D and thermal conduction in the droplet and in air, $\tau_{\lambda d}$ and $\tau_{\lambda gas}$, respectively, are much smaller than the characteristic flow residence time of the droplet, τ_{fd}, which depends on how fast the droplet is traveling along the x-axis. Using the following expressions for above time scales, $\tau_{fd} = \overline{\Delta x} / V_{d,max}$, $\tau_D = d^2/\overline{D}$, $\tau_{\lambda d} = \rho_d c_{p_d} R_d^2/\lambda_d$, and $\tau_{\lambda gas} = \overline{\rho c_p} d^2/\overline{\lambda}$, where overlined properties identify averaged quantities around the droplet (see Appendix A). Here, $\overline{\Delta x}$ is a characteristic length along the x-axis, where gas-phase temperature and vapor mass fraction vary appreciably, λ_d is the thermal conductivity of liquid water, and $V_{d,max}$ is the maximum value of velocity of the droplet in its trajectory.

Estimation of the characteristic time scales described above from the converged numerical solution indicates that $\tau_{\lambda d}$ is definitely larger

than τ_{hd}. Thus, the assumption of uniform temperature field within the droplet is expected to be invalid. However, the error introduced in the solution is not large because the fraction of energy flux that goes into raising the temperature of the droplet is typically of an order of magnitude less than that associated with latent heat of evaporation, especially for the size of droplets considered here. In addition, small error in T_s (the droplet temperature at the surface for nonuniform droplet temperature) is expected to introduce negligible influence on the mass evaporation rate as $T_\infty \gg T_s$. This can be better demonstrated by writing the mass evaporation rate in terms of the transfer number based thermal driving force, Q', given by [8, 10]

$$Q' = 2\pi d \frac{\lambda}{c_p} \ln \left[1 + \frac{c_p(T_\infty - T_s)}{L} \right] \quad (31)$$

Therefore, the profiles of the source terms of mass and enthalpy are hardly affected by the above errors. Certainly, the comparison of characteristic time scales indicates the need for more-accurate modeling of the internal heat transfer, especially for larger droplets such as those encountered in water sprinklers.

Sensitivity of the Solutions to F_x, Q, and H

Besides the deficiencies in droplet evaporation and heat transfer modeling described above, the estimation of the body force F_x may involve some uncertainties, primarily associated with the neglect of gravity and low Reynolds number approximation for the viscous drag force. For the high-strain rate flows considered here, it is relatively easy to establish the negligible role of gravity based on the ratio of potential energy to kinetic energy, given by $2g(x_u - x_f)/v_{f0}^2 \approx 10^{-5}$.

According to Refs. [2, 10, and 11] the models developed assuming quiescent atmospheric conditions underestimate evaporation and heat transfer by ~25% and drag coefficients by ~15% for large droplets when $Re_d \gg 1$. However, no mention is made about possible effects of mass evaporation on drag or its interaction with convection effects at high Re_d. For the conditions considered here, however, the maxi-

The Sensitivity of a_{ext} to Variation of F_x, Q, and H for $d = 30~\mu m$, $Y_0 = 3\%$

Δ (%)	$F_x = F_x(1 + \Delta)$ (%)	$Q = Q(1 + \Delta)$ (%)	$H = H(1 + \Delta)$ (%)
-20	0.9	-7.3	-8.7
$+20$	$+1.1$	2.8	-8.5

mum observed Re_d is about 2.5 for $d = 50~\mu m$ and $Y_0 = 1\%$ near extinction, whereas, for all the other cases, it is equal to or less than 1. It should also be pointed out that high Re_d effects cannot be directly included in the current modeling approach, as Q, H, and F_x would end up depending on r_d and the source terms themselves on r, invalidating the hypothesis used in defining the self-similar solution. One way to overcome such a difficulty is by assuming $Re_{d_r} \gg Re_{d_x}$, where Re_{d_r} and Re_{d_x} are Reynolds numbers based on the axial and radial velocity components of the droplet, respectively. Then F_r, F_x, Q, and H are modified by factors of the kind $1 + \alpha Re_{d_r}^\beta$, where α and β are constants $\ll 1$ [4]. Such an assumption may be considered valid only near the x-axis, when the gas-phase flow is given as in Eq. 1.

Before undertaking the challenging task of improving the submodels used, the sensitivities of any possible errors associated with F_x, Q, and H are assessed here. For the case with $d = 30~\mu m$ and $Y_0 = 2\%$, the modification of F_x, Q, and H by $\pm 20\%$ on the predicted extinction strain rate is shown in Table 3. It is evident that large errors on the axial force estimations do not particularly affect a_{ext}, at least as long as the force is strong enough to make the droplets follow the gas well. The small increase in a_{ext} for positive ΔF_x is due to the fact that near the flame the gas accelerates, dragging the droplets with itself before slowing down again at the stagnation flame as can be seen in Fig. 4. Errors in both Q and H appear to affect the solution more significantly. In the case of modified Q, the lower variation on a_{ext} for $\Delta = +20\%$ is perhaps due to the coupled effect of Q on F_x and H, which reduces the droplet size rapidly to the 15-μm range. In case of modified H, the variation of a_{ext} is the same for both signs of Δ. The a_{ext} is more sensitive to H not only because
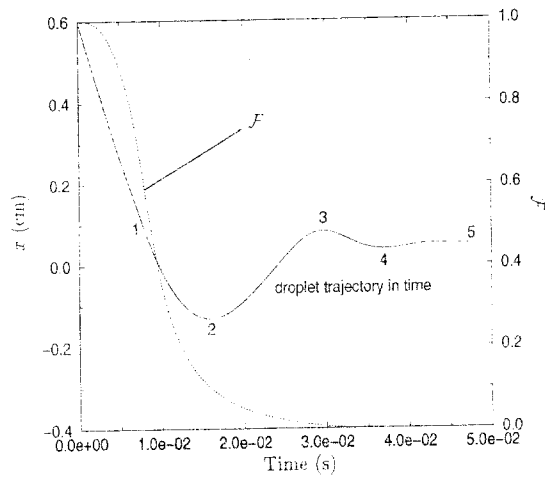
Fig. 18. Droplet trajectory as a function of time, for $d = 50$ μm and $Y_0 = 0.03$.

of the modification of Q by changing the equilibrium temperature but also because of the rapid increase in T_d before the droplet reaches the flame.

Droplet-Droplet Collisions

A key assumption in the numerical model developed is that droplets are transported without collision with others. This assumption allows for a fairly simple description of the droplet flow field and derivation of a self-similar solution for both droplets and gas phase. It relies on the idea that the droplets leaving the air nozzle are monodisperse with the same exit velocity (v_{do}), hence, similar dynamics in the counterflow field. Although such ideal conditions are difficult to be realized in experimental situations, if the initial droplet separation distance to droplet diameter is large, as seen by Table 1, the fraction of droplets colliding before evaporation can be neglected.

The worst situation that can violate this assumption arises when large droplets with high droplet loading penetrate the stagnation plane and reverse their trajectory, creating a region where opposed flow of droplets exists near the axis of symmetry. Such a region exists for 50-μm droplets considered here, as seen in Fig. 5. Figure 18 shows the calculated trajectory of such 50-μm droplets along the x-axis as a function of time and the corresponding flux fraction

function for $Y_0 = 3\%$. With $v_{do} = 60$ cm/s and an average distance $l_0 = 24d = 0.12$ cm (see Table 1), each droplet is estimated to be preceded and followed by a droplet before and after a time 1.8×10^{-3} s. Thus, if it is assumed that droplets are leaving the air nozzle at every 1.8×10^{-3} s, then the region between points 1 and 2 (the region where each droplet group would see a group of droplets flowing in the opposing direction) in Fig. 18 consists of ~17 layers. By taking the average value of droplet flux fraction, $\mathcal{F}$, in region $1 \rightarrow 2$ as $1/2$ and in region $2 \rightarrow 3$ as $1/4$, the probability of droplet collision in this worst case region can be roughly estimated as

$$P_{coll} \sim 17 \frac{1}{2} \frac{1}{4} \left(\frac{d}{l_0}\right)^2 \approx 0.4\% \quad (32)$$

Clearly, this estimate for collision probability gets even smaller for smaller droplets because of evaporation and the increased straining of droplet flux. Hence, the assumption of negligible droplet collision is reasonable.

SUMMARY AND CONCLUDING REMARKS

The purpose of this work was to develop a new two-phase numerical model to analyze the effectiveness of monodisperse condensed-phase fire suppressants in extinguishing counterflow flames. An important feature of the new model developed is it can overcome the singularities associated with solving the droplet number density equation in counterflow field accurately and in a very robust manner. This was achieved by using a hybrid Eulerian–Lagrangian formulation for the gas–droplet flow, with the introduction of droplet flux fraction to describe the droplet number density equation.

As part of this work, the model developed was applied to a case where monodisperse water droplets are introduced with the air stream to a nonpremixed counterflow flame of methane and air. Several cases with different droplet sizes, ranging from 5–50 μm, were considered. Small droplets (<20 μm) tend to follow the gas closely and go through rapid evaporation in the hot mixing layer, and it was shown that they never cross the stagnation plane. The 50-μm droplet considered was shown to cross the stagnation

plane several times, before being completely vaporized. The most important finding of the present work is that the flame extinction strain rate shows nonmonotonic behavior for different monodisperse droplet sizes considered for several water mass loadings (1–3% in condensed phase). Assuming that the droplets leave the air stream at the same velocity as the gas, 15-μm droplets were seen to be the most effective. For example, addition of 3% of water by mass in condensed phase (in addition to 2.22% as saturated vapor) was shown to reduce the extinction rate to 134 s^{-1}, from about 400 s^{-1} for the dry case. The nonmonotonic effect of droplet size, especially the superior flame extinction phenomenon associated with 15-μm droplets, is attributed to the droplet dynamics in the counterflow field and to the large mass evaporation and heat sink observed near the oxygen consumption layer. A careful analysis of the physical, thermal, and chemical contributions controlling the phenomena predicted here is currently under way and will be presented in a separate paper.

Sensitivity analyses of the approximate analytical models used to simplify the numerical integrations show that mass evaporation and heat transfer terms need to be more accurately modeled. Methods of improving the accuracy of these models will be pursued in the future.

APPENDIX A

The Lagrangian equations describing the conservation of mass, momentum (both x and r directions), and enthalpy of a single droplet can be written as

$$\frac{dm_d}{dt} = -Q \tag{A1}$$

$$\frac{d}{dt}(m_d r_d) = -Q r_d + F_x \tag{A2}$$

$$\frac{d}{dt}(m_d u_d) = -Q u_d + F_r \tag{A3}$$

$$\frac{d}{dt}(m_d h_d) = -Q(h_d + L) + H \tag{A4}$$

where, m_d is the droplet mass, Q the mass evaporation rate, F_x the axial component of the external force acting on the droplet, F_r the radial component of the external force acting on the droplet, h_d the droplet specific enthalpy, H the heat flux from the gas to the droplet, and L the average heat of evaporation at the droplet surface.

The values of Q, F_x, F_r, and H depend in general on the state of the droplet, its relative motion with respect to the gas, the thermochemical and transport properties of the gas, and the presence of other droplets in the neighborhood. To accurately determine these terms, the regions around each droplet controlling the mass and heat transfer should be resolved. Fortunately, water vapor mass fraction, temperature, velocity, and thermodynamic coefficients of the gas around the droplet vary over distances greater than few diameters. Thus, average values of these gas-phase variables are used to determine Q, F_x, F_r, and H.

Simplified Models for Evaporation, Heat Transfer, and Forces Acting on the Droplet

When droplets are not at rest relative to the surrounding gas phase, convection affects evaporation and heat transfer. This effect can be assessed by estimating the droplet Reynolds number defined as

$$Re_d = \frac{\rho V_d d}{\mu} \tag{A5}$$

where ρ is the density averaged in the region around the droplet, μ the viscosity averaged in the region around the droplet, $V_d = ((v_d - v)^2 + (u_d - u)^2)^{1/2}$, and d the diameter of the droplet. When $Re_d > 20$, there exists a boundary-layer flow region around the front of the droplet and a wake region behind it [11], and therefore the droplets can interfere with each other. When Re_d is of the order of 100 or higher, the shear stress at the gas-liquid interface can be large enough to induce internal liquid-phase circulation [10, 11]. However, if the

droplets are very small, as considered here, such effects can be neglected.

In the counterflow under consideration, the estimated Re_d is of the order of 1 or less (at least near the x-axis) so that the approximation of droplets in quiescent atmosphere can be adopted. To get to a simplified and explicit analytical solution for Q and H, the following is assumed: (1) the temperature and diffusion fields are spherical-symmetric, (2) pressure is constant, equal to p_0, (3) the droplets are sufficiently far apart such that their evaporation and heat transfer occurs as in a single isolated droplet, (4) boundary conditions at infinity of the surrounding gas of each single droplet are given by the gas phase T and Y_k's at the droplet location, (5) evaporation and heat transfer are quasisteady (i.e., the droplet diameter, temperature, etc. are assumed to vary slowly relative to the transients of the gas properties around the droplet), (6) the gas surrounding the droplet is treated as a binary mixture of the evaporating species and a gas whose thermodynamic properties are the same as a uniform mixture of the other nonevaporating species present in the gas phase at the droplet location, and (7) chemical reactions in the regions around each droplet are neglected (i.e., the evaporated species affects the chemical reaction in the gas phase only through the source term in Eq. 3). Integration of equations for mass, diffusion, and enthalpy of such single isolated droplets yield the following expressions for mass evaporation and heat transfer:

$$Q = 2\pi d \frac{\bar{\lambda}}{\bar{c}_p \overline{Le}_i} \ln\left(\frac{1 - Y_i}{1 - Y_{i_s}} \right) \qquad (A6)$$

$$H = 2\pi d \bar{\lambda}(T_\infty - T_s) \frac{Q\bar{c}_p/2\pi d\bar{\lambda}}{[\exp(Q\bar{c}_p/2\pi d\bar{\lambda}) - 1]} \qquad (A7)$$

where subscript i indicates the evaporating species (in this case water), and s and ∞ indicate the conditions at the droplet surface and ∞, respectively. The gas properties with overbar are evaluated using the standard 1/3 law [10]. Here, $\overline{Le}_i = (\bar{\lambda}/\overline{\rho c_p})/\overline{D}_{im}$ is the Lewis number based on averaged properties, with $\overline{D}_{im}$ being the overall diffusivity of the evaporating species into the mixture.

The force components F_x and F_r include viscous drag forces due to droplet motion relative to the gas phase and evaporation rate. Gravity effects are neglected here because of the high convective velocities. As Re_d is of the order of 1 or less, the force components are approximated assuming Stokes drag coefficient $C_D = 24/Re_d$, which yields

$$F_x = 3\pi d\bar{\mu}(v - v_d) \qquad (A8)$$

$$F_r = 3\pi d\bar{\mu}(u - u_d) \qquad (A9)$$

The equations above allow the existence of a self-similar solution for the single droplet equations.

Self-Similar Formulation of Droplet Dynamics

For the gas-phase flow field written in the form of Eq. 1, when Q, H, F_x, and F_r are given in Eqs. A6–A9, the right-hand sides of Eqs. A1, A2, and A4 depend only on x_d, the droplet axial coordinate, whereas the right-hand side of Eq. A3 is proportional to r_d, the droplet radial coordinate. In Ref. [2], a new variable $s = r_d/u_{d_o}$ was introduced to cast the system of equations in a self-similar form, with $s_o = 1 =$ constant for the potential flow field considered with a defined as the flow strain rate and subscript 0 identifying the conditions at the inflow plane. For the general rotational flow formulation considered here, with the flow strain rate varying from zero at the air inflow plane (i.e., for plug flow) to some finite value near the mixing layer, assuming

$$u_d = U_d(t)r_d \qquad (A10)$$

the system (A1)–(A4) can be reduced to a system of ODE's independent from r_d, so that the trajectories of all the droplets can be determined with a single integration in time. With these simplifications, the system of Eqs. A1–A9 together with the equations for the droplet location can be written as

$$\frac{dx_d}{dt} = v_d \qquad (A11)$$

$$r_d = r_{d_o}R(t) \qquad (A12)$$

$$\frac{dm_d}{dt} = -Q \tag{A13}$$

$$\frac{d}{dt}(m_d v_d) = -Q v_d + 3\pi d\bar{\mu}(v - v_d) \tag{A14}$$

$$\frac{d}{dt}(m_d U_d) + m_d U_d^2 = -Q U_d + 3\pi d\bar{\mu}(U - U_d) \tag{A15}$$

$$\frac{d}{dt}(m_d h_d) = -Q(h_d + L) + H \tag{A16}$$

where $\mathfrak{R}(t) = \exp(\int_{t_0}^t U_d(t)dt)$ is a function of t only. The initial conditions are

$$x_d(t_0) = x_0, \ r_d(t_0) = r_{d_0}$$

$$v_d(t_0) = v_{d_0}, \ U_d(t_0) = U_{d_0}$$

$$d(t_0) = d_0, \ T_d(T_0) = T_{d_0} \tag{A17}$$

where T_d is the droplet temperature, assumed to be uniform.

Equations A13–A16 can be further simplified by introducing an averaged droplet specific heat, c_{pd}, and liquid density, ρ_d (independent of T_d), so that

$$h_d = c_{p_d}(T_d - T_0) + h_{d_0} \tag{A18}$$

$$m_d = \frac{\pi}{6}\rho_d d^3 \tag{A19}$$

where h_{d_0} is the droplet specific enthalpy at the reference temperature T_0. Then, use of Eqs. A6, A7, A18, and A19 in Eqs. A13–A16 yields the simplified set of Eqs. 9–13 described previously.

REFERENCES

1. Grosshandler, W. L., Gann, R. G., and Pitts, W. M. (1994) Publ. *SP-861*, National Institute of Standards and Technology, Gaithersburg, MD.

2. Continillo, G., and Sirignano, W. A., *Combust. Flame* 81:325 (1990).

3. Lacas, F., Darabiha, N., Versaevel, P., Rolon, J. C., and Candel, S., (1992) *Twenty-Fourth Symposium (International) on Combustion*, The Combustion Institute, Pittsburgh, p. 1523.

4. Chen, N.-H., Rogg, B., and Bray, K. N. C. (1992) *Twenty-Fourth Symposium (International) on Combustion*, The Combustion Institute, Pittsburgh, p. 1513.

5. Li, S. C., Libby, P. A., and Williams, F. A., *Combust. Flame* 94:161 (1993).

6. Chelliah, H. K., Law, C. K., Ueda, T., Smooke, M. D., and Williams, F. A., (1990) *Twenty-Third Symposium (International) on Combustion*, The Combustion Institute, Pittsburgh, p. 503.

7. Seshadri, K., *Combust. Flame* 33:197 (1978).

8. Williams, F. A., *Combustion Theory*, 2nd ed., Addison Wesley, Reading, MA, 1985.

9. Kuo, K. K., *Principles of Combustion*, Wiley-Interscience, New York, 1986.

10. Law, C. K., *Prog. Energy Combust. Sci.* 8:171 (1982).

11. Abramzon, B., and Sirignano, W. A., *Int. J. Heat Mass Transfer* 32(9):1605 (1989).

12. Kee, R. J., Miller, J. A., Evans, G. H., and Dixon-Lewis, G., (1988) *Twenty-Second Symposium (International) on Combustion*, The Combustion Institute, Pittsburgh, p. 1479.

13. Smooke, M. D., Crump, J., Seshadri, K., and Giovangigli, V., (1990) *Rep. ME-100-90*, Yale University, New Haven, CT.

14. Seshadri, K., and Williams, F. A., *Int. J. Heat Mass Transfer* 21:251 (1978).

15. Smooke, M. D., *J. Comp. Phys.* 48:72 (1982).

16. Miller, J. A., Kee, R. J., Smooke, M. D., and Grear, J. F., (1984) The Computation of the Structure and Extinction Limit of a Methane-Air Stagnation Point Diffusion Flame, The Combustion Institute, Pittsburgh.

17. Smooke, M. D., Puri, I. K., and Seshadri, K., (1986) *Twenty-First Symposium (International) on Combustion*, The Combustion Institute, Pittsburgh, p. 1783.

18. Kee, R. J., Rupley, F. M., and Miller, J. A. (1993) *Chemkin II: A Fortran Chemical Kinetics Package for the Analysis of Gas Phase Chemical Kinetics*, Rep. *SAND89-8009B*, Sandia National Laboratories, Livermore, CA.

19. Kee, R. J., Dixon-Lewis, G., Warnatz, J., Coltrin, M. E., and Miller, J. A., (1992) *A Fortran Computer Code Package for the Evaluation of Gas-Phase Multicomponent Transport Properties*, Rep. *S6-8246*, Sandia National Laboratories, Livermore, CA.

20. Peters, N., and Rogg, B., *Lecture Notes in Physics*, Vol. m15, Springer-Verlag, New York, 1993.

21. Vargaftik, N. B., *Tables on the Thermophysical Properties of Liquids and Gases*, Hemisphere, New York, 1975.

22. Seshadri, K., and Peters, N., *Combust. Flame* 73:23 (1988).

23. Chelliah, H. K., and Williams, F. A., *Combust. Flame* 60:17 (1990).

24. Peters, N., *Combust. Sci. Technol.* 30:1 (1983).

25. Kim, J. S., and Williams, F. A., *SIAM J. Appl. Math.* 53(6):1551 (1993).